# Changes in Anthropogenic $PM_{2.5}$ and the Resulting Global Climate Effects Under the RCP4.5 and RCP8.5 Scenarios by 2050

Dongdong Yang, Hua Zhang, & Jiangnan Li

December 2019

Earth's Future

RESEARCH ARTICLE
10.1029/2019EF001285

**Key Points:**
- $PM_{2.5}$ decreases over most continents, coarse particles decrease by regions
- ERF increases 1.17 (1.10) W $m^{-2}$ for $PM_{2.5}$, but changes slightly for CPM
- Climate responses to particle changes under RCP4.5(8.5) were quantified

**Supporting Information:**
- Supporting Information S1

**Correspondence to:**
H. Zhang,
huazhang@cma.gov.cn

**Citation:**
Yang, D., Zhang, H., & Li, J. (2020). Changes in anthropogenic $PM_{2.5}$ and the resulting global climate effects under the RCP4.5 and RCP8.5 scenarios by 2050. *Earth's Future*, *8*, e2019EF001285. https://doi.org/10.1029/2019EF001285

Received 13 JUN 2019
Accepted 7 DEC 2019
Accepted article online 11 DEC 2019

**Author Contributions**
**Writing - Original Draft:** Dongdong Yang
**Formal Analysis:** Jiangnan Li
**Writing - review & editing:** Dongdong Yang, Jiangnan Li



# Changes in Anthropogenic $PM_{2.5}$ and the Resulting Global Climate Effects Under the RCP4.5 and RCP8.5 Scenarios by 2050

**Dongdong Yang[1,2], Hua Zhang[1,2], and Jiangnan Li[3]**

[1]State Key Laboratory of Severe Weather, Chinese Academy of Meteorological Sciences, Beijing, China, [2]Collaborative Innovation Center on Forecast and Evaluation of Meteorological Disasters, Nanjing University of Information Science and Technology, Nanjing, China, [3]Canadian Center for Climate Modeling and Analysis, University of Victoria, Victoria, British Columbia, Canada

**Abstract** Using an aerosolclimate model, we studied the temporal and spatial variations of anthropogenic $PM_{2.5}$ (aerodynamic diameter ≤2.5 μm) and coarse particulate matter (CPM; aerodynamic diameter >2.5μm) under Representative Concentration Pathway (RCP) 4.5 and RCP8.5 scenarios from 2014 to 2050. The corresponding radiative forcing and climate responses were also explored. The $PM_{2.5}$ burden decreases over most continents, especially East Asia. The CPM particles increase over northern Asia, North America, and central Africa, in contrast to decrease over most regions of East Asia and North Africa. Relative to 2014, the global annual mean effective radiative forcing due to changes in $PM_{2.5}$ and CPM burden are 1.17 (1.10) and −0.06 (−0.07) W $m^{-2}$ under RCP4.5 (RCP8.5), respectively. The reduction in $PM_{2.5}$ burden leads to apparent warming, especially over high latitudes of the Northern Hemisphere, with global annual mean surface air temperature increasing by 1.25 K under RCP4.5, and 1.22 K under RCP8.5. In contrast, changes in CPM result in apparent cooling over North America and northern Asia, with global annual mean changes in surface air temperature of 0.10 K for both scenarios. The Northern Hemisphere Hadley cell weakens and moves northward due to changes in $PM_{2.5}$ after 2014, whereas the corresponding circulation in the Southern Hemisphere is strengthened, with the Intertropical Convergence Zone shifting to 10°N. Global annual mean precipitation increases by 0.10 mm $day^{-1}$ under both scenarios. Generally, anthropogenic $PM_{2.5}$ contributes significantly to future changes in radiative forcing and climate.

## 1. Introduction

Atmospheric air pollutants are currently increasing sharply due to the intensification of human activities. Numerous studies have shown that not only can anthropogenic aerosol particles affect the environment and human health, directly changing the radiation balance of the Earth system (Bond et al., 2013; Zhang et al., 2012, 2014). They can also have apparent indirect influences on the climate (Kloster et al., 2010; Zhang, 2007). The Fifth Assessment Report of the Intergovernmental Panel on Climate Change defined effective radiative forcing (ERF) as change in the top of atmosphere (TOA) radiation balance, under conditions of fixed global mean surface temperature or ocean and sea ice properties as well as changes in atmospheric temperature, water vapor, clouds, and land albedo in response to changes in aerosol radiative processes (Myhre et al., 2013). Zhang et al. (2016) showed that the global annual mean ERF of sulfate (SF), black carbon (BC), and organic carbon (OC) from 1850 to 2010 were −2.37, 0.12, and −0.31 W $m^{-2}$, respectively, based on an aerosolclimate coupled model (BCC_AGCM2.0_CUACE/Aero) (Zhang et al., 2012). Since the preindustrial era, the increasing anthropogenic aerosols have played an essential role in global climate change. Bollasina et al. (2011) indicated that anthropogenic aerosols were likely the major contributor to the reduction in precipitation over South Asia. Hu and Liu (2013) found that anthropogenic aerosols supported a decrease in late spring precipitation in South China from the year 1950 to 2000. Rotstayn and Lohmann (2002) showed that horizontally inhomogeneous distributions of aerosol forcings could have dynamic effects on atmospheric circulation due to horizontal gradients in the forcing. The dynamic effects of long-term rising aerosol concentrations have been described as a southward shift in the Intertropical Convergence Zone (ITCZ) or changes in Hadley cells in both the Northern Hemisphere (NH) and Southern Hemisphere (SH) (Ming &

Ramaswamy, 2011; Williams et al., 2001), which could be due primarily to interhemispheric asymmetry in aerosol forcings (Chiang & Friedman, 2012).

Based on the projections of reductions in aerosols during the 21st century (Bond et al., 2013; Rotstayn et al., 2013), climate change scenarios Representative Concentration Pathway (RCP) 4.5 and 8.5 both predict a decrease in the anthropogenic aerosol concentration over the rest of this century. Efforts to reduce aerosol burden are broadly understood to aggravate future increases in global annual mean atmospheric temperature, due to reduced scattering of solar energy back to space by aerosols. Aerosols always contain a distribution of sizes, and their scattering and absorption characteristics vary according to this size distribution (Li et al., 2001, 2015; Srivastava et al., 2011). Furthermore, aerosol size distribution is associated with specific air pollutants. Public awareness of air pollution has been growing due to continuous increases in air pollutant concentrations, especially that of anthropogenic $PM_{2.5}$. $PM_{2.5}$ refers to atmospheric particulate matter (PM) with a particle diameter less than or equal to 2.5 μm. Particles of this fine size class tend to remain in the air longer than coarse particles. Both the small size and long life span of fine particles increase their chance of being inhaled into the human body.

It is shown that the changes in anthropogenic $PM_{2.5}$ can have an impact on the global climate (Fu et al., 2016; Wang, Wang, et al. 2017). Lecœur et al. (2014) used different model predictions to study climate change and estimate future levels of $PM_{2.5}$ burden. So et al. (2014) indicated that changes in $PM_{2.5}$ concentrations over East Asia might significantly influence climate variability over the North Pacific by altering the cloud fraction and atmospheric circulation. However, the climate impact of $PM_{2.5}$ cannot be addressed without considering its counterpart, coarse particulate matter (CPM), as the two always occur together. Here, CPM refers to particles with diameters larger than 2.5 μm. Some studies show the roles of both $PM_{2.5}$ and CPM in past climate changes from the preindustrial period to the present. $PM_{2.5}$ results in stronger isotropic scattering, and greater reflection of the solar radiation, whereas CPM causes stronger forward scattering with less reflection. Therefore, CPM particles produce a smaller cooling effect in the atmosphere compared to $PM_{2.5}$ particles. Furthermore, Li et al. (2001) showed that larger particles have stronger solar absorption compared to smaller particles, which also contributes to the positive radiative forcing of CPM. Therefore, $PM_{2.5}$ and CPM usually played opposite roles in past climate changes.

Despite efforts to identify climate changes due to decreased anthropogenic aerosols, in studies of future climate change based on RCP4.5 or RCP8.5, the role of the aerosol size distribution has seldom been addressed. In most current global climate models, the aerosol size distribution is not well resolved due to the use of a bulk aerosol scheme. BCC_AGCM2.0_CUACE/Aero is among the advanced climate models with well-resolved aerosol size distributions, with each type of aerosol classified into 12 bins following a geometric series of radius lengths between 0.005 and 20.48 μm. The primary purpose of this study is to study the evolution of the aerosol size distribution and its climate impacts under future climate scenarios by using BCC_AGCM2.0_CUACE/Aero. We separately address $PM_{2.5}$ and CPM as fine and coarse anthropogenic aerosols at the global scale under climate change scenarios RCP4.5 and RCP8.5 from the year 2014 to 2050 with the aim of elucidating the roles of particles of the two size classes in air pollution, radiative forcing, and climate change.

In section 2, we introduce the aerosol climate coupled model, data used in this study, and the experimental design. Section 3 presents simulated temporal and spatial variations in anthropogenic $PM_{2.5}$ and CPM column concentrations under RCP4.5 and RCP8.5 scenarios from 2014 to 2050. Analysis of related radiative forcings at TOA/surface, energy transport, and corresponding climatic effects caused by changes in the $PM_{2.5}$ and CPM burden, including changes in atmospheric temperature, atmospheric circulation, clouds, and precipitation are also presented in this Section. We conclude this study in Section 4 with a summary.

## 2. Methods

### 2.1. Model

An aerosolclimate online model, BCC_AGCM2.0_CUACE/Aero, developed by Zhang et al. (2014) and Wang et al. (2014), was used in this study. BCC_AGCM2.0_CUACE/Aero was constructed by coupling the atmospheric general circulation model, Beijing Climate Center Atmospheric General Circulation Model 2.0 (BCC_AGCM2.0) (Wu et al., 2008, 2010), with the China Meteorological Administration Unified Atmospheric Chemistry Environment for Aerosols aerosol module (CUACE/Aero) (Wang et al., 2014; Zhang et al., 2012, 2014; Zhou et al., 2012). Based on the Eulerian spectral formulation of the dynamic equations,

**Table 1**
*Experimental Design*

| Group | Test name | Emissions data | Sea temperature | Runn length |
|---|---|---|---|---|
| 1 | ERF_$PM_{2.5}$_0 | | | |
| | ERF_TPM_0 | SF, BC, and OC of 1850 | | |
| | ERF_$PM_{2.5}$_1 | | | |
| | ERF_TPM_1 | SF, BC, and OC of 2014 | Prescribed SST and SI | 30 |
| | ERF_$PM_{2.5}$_2 | | | |
| | ERF_TPM_2 | SF, BC, and OC of 2050 | | |
| 2 | CLI_$PM_{2.5}$_1 | | | |
| | CLI_TPM_1 | SF, BC, and OC of 2014 | | |
| | CLI_$PM_{2.5}$_2 | | Coupled SOM | 80 |
| | CLI_TPM_2 | SF, BC, and OC of 2050 | | |

the BCC_AGCM2.0 employs a horizontal resolution of T42 (approximately 2.8 * 2.8) and a 26-layer hybrid sigma pressure coordinate in the vertical direction, with the top located at approximately 2.9 hPa.

CUACE/Aero considers five types of aerosols, including anthropogenic aerosols (SF, BC, and OC) and natural aerosols (SS and SD). Emissions of the three types of anthropogenic aerosols are input offline, and emissions of the two natural aerosols are calculated online in the aerosol module. Each type of aerosol is divided into 12 bins as a geometric series with the radius lengths between 0.005 and 20.48 μm, which can be used to estimate the radiative forcing and climatic effects caused by particles of different sizes. Additionally, transportation, chemical transformations, cloud interactions, and aerosol removal processes are also considered in the module (Zhou et al., 2012).

Direct, semidirect, and indirect aerosol effects are included in BCC_AGCM2.0_CUACE/Aero (Wang, Zhang, Li, et al. 2013, 2014; Zhang et al., 2012). Wang et al. (2014) incorporated a two-moment bulk cloud microphysical scheme to study aerosol radiation and aerosolcloud interactions, along with their climatic effects. The Monte Carlo Independent Column Approximation (McICA) scheme developed by Räisänen et al. (2004) was applied to the model to resolve subgrid cloud variability. Previous studies have shown that this model simulates aerosol mass concentrations, optical properties, and climatology well (Zhang et al., 2012; Yang et al., 2016, 2017). The model has been used to study radiative forcing due to aerosols (Bond et al., 2013; Myhre et al., 2013; Wang, Zhang, Li, et al. 2013; Wang, Zhang, Jing, et al. 2013; Zhang et al., 2012, 2016) and its effects on climate (Wang, Wang, et al. 2017; Zhang et al., 2016; Zhao et al., 2017; Zhou et al., 2017). Moreover, results of the model continue to be included in the Aerosol Comparisons Between Observations and Models (AeroCom) project database (Myhre et al., 2013; Sand et al., 2017).

### 2.2. Experimental Design

The RCPs comprise a set of greenhouse gas concentrations and emissions pathways designed to support scientific research into the effects and potential policy responses to global climate change (Moss et al., 2010; Van Vuuren & Riahi, 2011). RCP4.5 corresponds to a radiative forcing pathway of 4.5 W $m^{-2}$ (approximately 650 ppm $CO_2$ equivalent) by the year 2100 without ever exceeding that value; RCP8.5 follows a rising radiative forcing pathway reaching 8.5 W $m^{-2}$, based on high greenhouse gas emissions (approximately 1370 ppm $CO_2$ equivalent) by the year 2100 (Van Vuuren & Riahi, 2011) and is regarded as the upper bound of RCPs. Here, we use the aerosol emissions under both the RCP4.5 and RCP8.5 scenarios to investigate the corresponding radiative and climatic effects of particles.

According to the classification of particle size in the coupled model used in this study, the first eight bins of total particulate matter (TPM) contain fine particles with aerodynamic diameters less than 2.5 μm, including anthropogenic $PM_{2.5}$ (hereafter, $PM_{2.5}$ refers to the sum of SF, BC, and OC particles in the first eight bins). The remaining four bins represent CPM, with aerodynamic diameters larger than 2.5 μm. SF($PM_{2.5}$)/BC($PM_{2.5}$)/OC($PM_{2.5}$) and SF(CPM)/BC(CPM)/OC(CPM) particles are defined in the same manner.

Two groups of experiments (Table 1) were conducted to calculate the ERF and climatic responses due to $PM_{2.5}$ and TPM burden changes under the RCP4.5 and RCP8.5 scenarios from 2014 to 2050. The ERF of

CPM is defined based on the difference between these values. Although the radiative and climatic effects of $PM_{2.5}$, CPM, and TPM may be nonlinear, climate states driven by TPM and $PM_{2.5}$ are similar. Thus, the climate state due to CPM can be considered a perturbation of the state due to TPM. Therefore, we used the differences between climate states driven by TPM and $PM_{2.5}$ to define the state of CPM. Emissions of anthropogenic aerosol particles and their precursors in 2014 were determined from Community Emissions Database System, a data set that provides a gridded historical inventory of climate-related anthropogenic aerosols for use in the Coupled Model Intercomparison Project Phase 6 (Hoesly et al., 2018). Emissions of aerosol particles and their precursors in 2050 were obtained from the Intergovernmental Panel on Climate Change RCP Database. Group 1 was used to calculate changes in ERF caused by $PM_{2.5}$ and CPM. Group 2 was used to simulate the corresponding climate effects. Test names appended with _0_1, and _2 indicate that emission data for the year 1850, 2014, and 2050, respectively, were used in the simulation. Each experiment was conducted twice, once each under the RCP4.5 and RCP8.5 scenarios.

In Group 1, each test was run over 30 years using the prescribed climatological monthly mean sea surface temperature and sea ice data (Hurrell et al., 2008), with results for the last 25 years used for the plotting and analysis. In Group 2, each test was run over 80 years and was coupled with a slab ocean model (Hansen et al., 1984) to calculate the responses of climate variables to varying $PM_{2.5}$ and CPM burdens from 2014 to 2050; results for the last 50 years were used to create plots and for analysis. Other conditions were the same in all experiments to ensure that the radiative forcing and climate effects were caused only by changes in the burdens of the three types of anthropogenic particles.

## 3. Results

### 3.1. Temporal and Spatial Variations in $PM_{2.5}$ and CPM

Figures 1 and 2 show the geographic distributions of changes in the column concentrations of $PM_{2.5}$ and CPM under the RCP4.5 and RCP8.5 scenarios from 2014 to 2050. In 2050, the simulated $PM_{2.5}$ burden is predicted to continue its apparent global decrease under RCP4.5 and RCP8.5, especially over middle and low latitudes in the NH, whereas the CPM loading is predicted to vary strongly among regions and shows small temporal changes over land and oceanic regions. Changes in the column concentrations of CPM are one or two orders of magnitude lower than those of $PM_{2.5}$. Therefore, the decrease in $PM_{2.5}$ burden gives rise to about 99% of the changes in column concentrations of total aerosol particles (sum of $PM_{2.5}$ and CPM burdens).

Under the RCP4.5 scenario, $PM_{2.5}$ column concentrations decrease over most regions, especially East Asia, the Arabian Peninsula, Indian Subcontinent, North America, and South Africa (Figure 1a). The global annual mean $PM_{2.5}$ column concentration is 4.71 mg $m^{-2}$ in 2014 and shows a decrease of 1.89 mg $m^{-2}$ by 2050 under the RCP4.5 scenario. We designate SF, BC, and OC particles with aerodynamic diameters smaller/larger than 2.5 μm as $SF(PM_{2.5})$/SF(CPM), $BC(PM_{2.5})$/BC(CPM), and $OC(PM_{2.5})$/OC(CPM), respectively. The global annual mean burdens of $SF(PM_{2.5})$, $BC(PM_{2.5})$, and $OC(PM_{2.5})$ decrease by 1.59, 0.07, and 0.23 mg $m^{-2}$ under RCP4.5, respectively. Decreases in the $SF(PM_{2.5})$ burden are distributed over most land areas and nearby oceanic areas, especially North America, South Africa, East Asia, the Arabian Peninsula, and Indian Subcontinent (Figure 1c), based on projections of reductions in anthropogenic aerosols. Decreases in the burdens of $BC(PM_{2.5})$ and $OC(PM_{2.5})$ occur over North America, East Asia, and the Indian Subcontinent (Figures 1e and 1g). However, in contrast to $SF(PM_{2.5})$, increases in $BC(PM_{2.5})$ and $OC(PM_{2.5})$ are predicted over central Africa and a few high-latitude regions of North America and North Asia. The increases in $BC(PM_{2.5})$ and $OC(PM_{2.5})$ column concentrations are attributed to regional increases in BC and OC sources and the combined effects of large-scale dynamics, which are discussed below.

Interestingly, patterns of changes in the CPM column concentration differs from those for $PM_{2.5}$. The global annual mean CPM column concentration increases by about 0.01 mg $m^{-2}$ under the RCP4.5 scenario for 2050. The different life spans of these particle classes cause the differing changes in $PM_{2.5}$ and CPM burdens. Generally, the lifetime of $PM_{2.5}$ is much longer than that of CPM; thus, existing $PM_{2.5}$ is more stable in the atmosphere compared to CPM, and the small column concentration of CPM can be more easily perturbed by the climate. Furthermore, aerosol particles can shift between size classes through numerous physical mechanisms, such as hygroscopic growth.

Changes in the column concentration of coarse particles vary among regions, with the burden increasing over northern Asia, North America, and central Africa, while it decreases over most regions of East Asia,

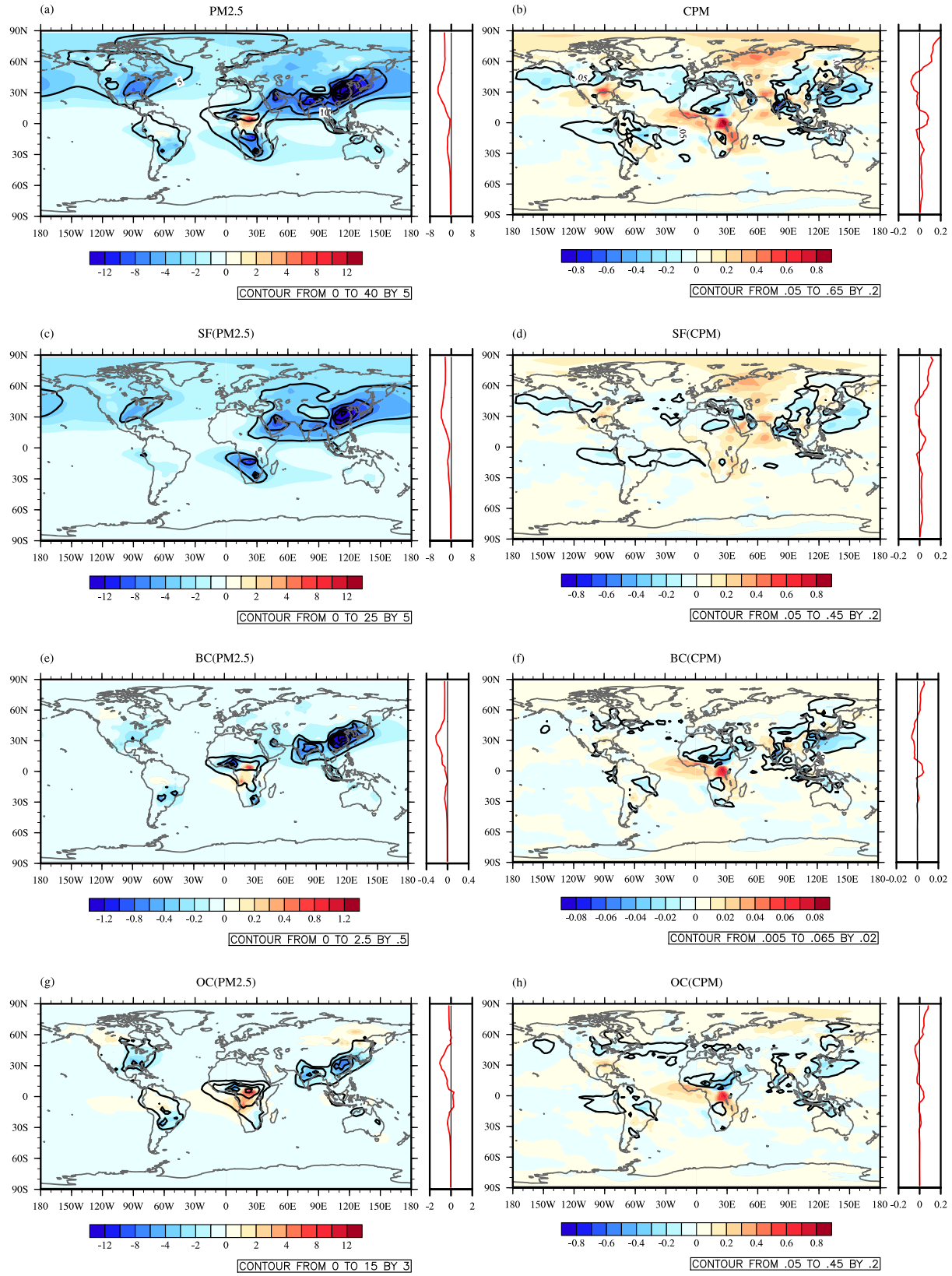


**Figure 1.** Global distributions of changes in annual mean column concentrations of anthropogenic $PM_{2.5}$ and CPM under the RCP4.5 scenario from 2014 to 2050 (units: mg $m^{-2}$). Panels (a), (c), (e), and (g) represent changes in the annual mean column concentrations of $PM_{2.5}$, $SF(PM_{2.5})$, $BC(PM_{2.5})$, and $OC(PM_{2.5})$, respectively; panels (b), (d), (f), and (h) represent for those of CPM, SF(CPM), BC(CPM), and OC(CPM), respectively.

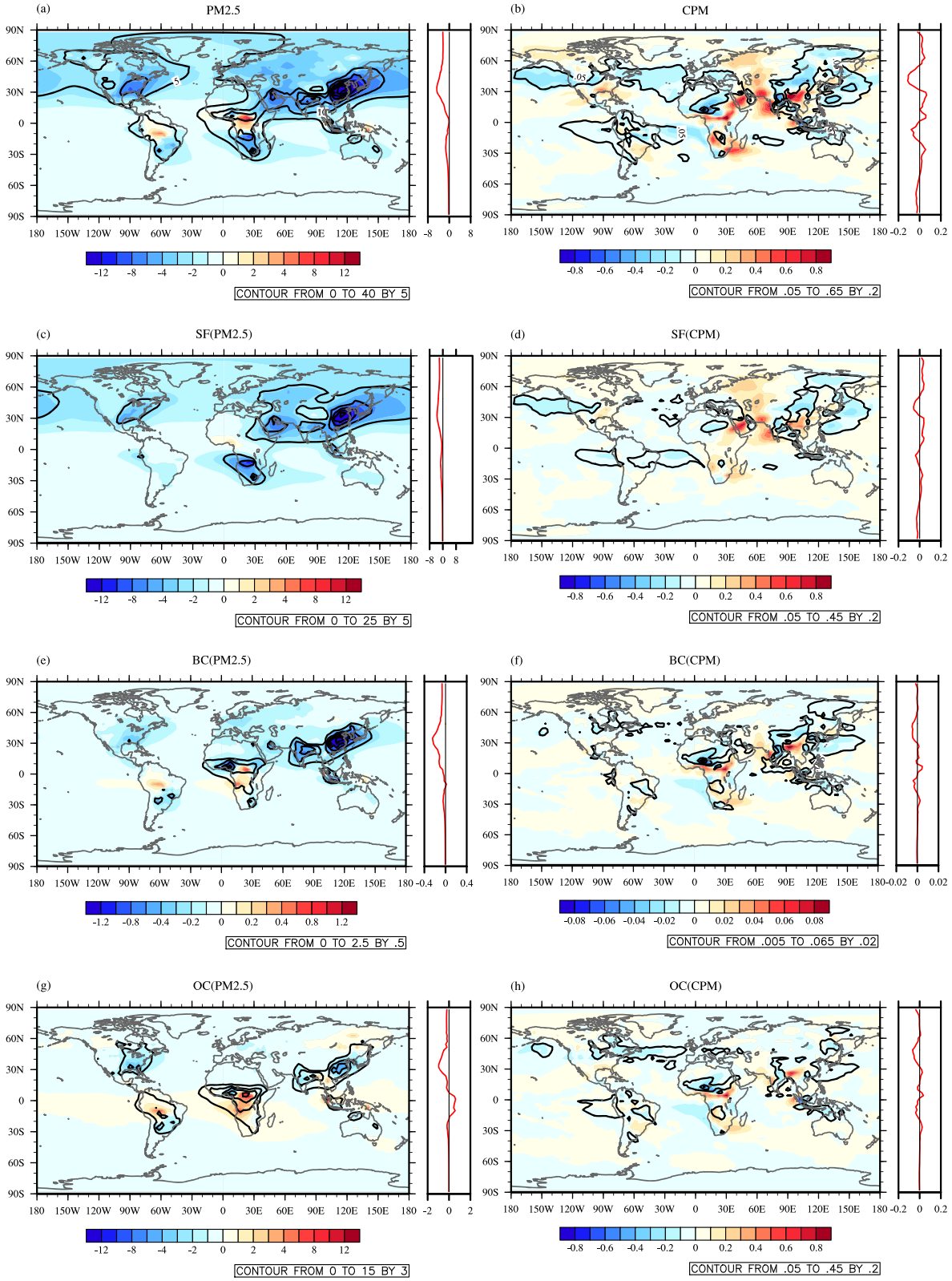


**Figure 2.** As described in Figure 1 but showing changes in the annual mean column concentrations of anthropogenic $PM_{2.5}$ and CPM under the RCP8.5 scenario from 2014 to 2050 (units: mg $m^{-2}$)

the Indian Subcontinent, and North Africa (Figure 2b). The increases over central Africa are mainly due to increasing BC(CPM) and OC(CPM), whereas the increases in the high latitudes of the NH are mostly caused by rising SF(CPM).

Under the RCP8.5 scenario, the geographic distributions of changes in $PM_{2.5}$ column concentrations are similar to the corresponding results under the RCP4.5 scenario (Figures 1 and 2). The global annual mean $PM_{2.5}$ column concentration decreases by 1.68 mg $m^{-2}$ under RCP8.5 in 2050, which is 11% lower than that under the RCP4.5 scenario. The greatest apparent difference occurs over northern South America, where an increase in $PM_{2.5}$ loading occurs under RCP8.5, mainly due to increased fine OC particles. The global annual mean burdens of SF($PM_{2.5}$), BC($PM_{2.5}$), and OC($PM_{2.5}$) decrease by about 1.48, 0.07, and 0.12 mg $m^{-2}$, respectively. The distributions of anthropogenic $PM_{2.5}$ components are also similar to those of RCP4.5.

For CPM, changes in the global annual mean column concentration are very small and negative (about −0.003 mg $m^{-2}$) under RCP8.5 from 2014 to 2050 and are smaller than those under RCP4.5. Over many areas, such as the high-latitude regions of the NH and South Africa along with neighboring oceanic regions, the geographic distributions of changes in CPM column concentrations under RCP8.5 clearly differ from those under RCP4.5. From the detailed component information, differences in the change in column concentration over the high-latitude region of the NH could be attributed to SF(CPM), and those in South Africa and the neighboring oceanic region mainly to OC(CPM) and BC(CPM).

### 3.2. Radiative Forcing and Energy Transport

#### 3.2.1. ERF

In this section, we study the ERF and surface net radiative flux (SNRF) due to anthropogenic $PM_{2.5}$ and CPM for both RCP4.5 and RCP8.5, which are the essential driving forces for the climatic change due to anthropogenic aerosols. Also, changes in corresponding energy transport are discussed, thereby helping us to understand the climate response to anthropogenic $PM_{2.5}$ and CPM shown in section 5.

Changes in radiative forcing associated with both $PM_{2.5}$ and CPM can help clarify the simulated climate responses in context. According to the experimental design described in section 2, we conducted a series of simulations forced by prescribed sea surface temperature and sea ice levels over 30 years to calculate the ERF (relative to 2014) that matches the changes in aerosol burden under these RCP future emissions scenarios. From its definition (Myhre et al., 2013), the ERF accounts for the differences in net radiative flux at TOA in the simulations using anthropogenic aerosols and precursor emissions for a given year (year 2050 in this study) minus those in 1850, which includes both indirect effects and rapid adjustments due to changes in aerosols (Shindell et al., 2013). Here, to elucidate of the climate changes induced by changes in fine and coarse particles in a future scenario beginning in 2014, the changes in ERF were calculated as the difference in net radiative flux at TOA from 2014 to 2050.

Figure 3 shows the geographic distributions of changes in annual mean ERF caused by the evolution of TPM, $PM_{2.5}$, and CPM from the year of 2014 to 2050 under both RCP4.5 and RCP8.5. Relative to 2014, the global annual mean ERFs due to the changing TPM is +1.11 W $m^{-2}$ under RCP4.5, and it is +1.03 W $m^{-2}$ under RCP8.5. The ERF of TPM is mainly located over low- and middle-latitude land and oceanic regions of the NH (Figures 3a and 3b). Global annual mean ERF from $PM_{2.5}$ is +1.17 W $m^{-2}$ under RCP4.5, and +1.10 W $m^{-2}$ under RCP8.5, both slightly larger than the values of TPM. The geographic distribution of ERF from $PM_{2.5}$ is similar to that from TPM in all emissions scenario (Figures 3a and 3c, and 3b and 3d).

Under RCP4.5, the geographical distributions of changes in ERF due to evolving $PM_{2.5}$ are similar to those under RCP8.5 (Figures 3c and 3d), and both are similar to the geographic distributions of the corresponding $PM_{2.5}$ column concentrations (Figures 1a and 2a), especially over land areas. Larger reductions in the aerosol loading are associated with larger increases in ERF. As shown by the zonal mean curves, the main difference between the two scenarios occurs in the middle latitudes of the NH, as evidenced by the critical factor of reduction in anthropogenic aerosol emissions over East Asia. Relative to 2014, the largest positive ERFs are located over East Asia, reaching 8.14 W $m^{-2}$ under RCP4.5, and over North America, reaching 7.88 W $m^{-2}$ under RCP8.5. As shown in Figure 1, changes in the $PM_{2.5}$ column concentration can be attributed mostly to reductions in SF($PM_{2.5}$) and OC($PM_{2.5}$). The positive ERF in 2050 is primarily caused by a decrease in the scattering effect, as strong scattering is a characteristic of SF($PM_{2.5}$). OC($PM_{2.5}$) is also a type of scattering aerosol, but its scattering characteristic is weaker than that of SF($PM_{2.5}$). Although the column concentrations of the strong absorbing particles, BC($PM_{2.5}$), decrease during this period, their limited negative radiative forcing could be offset by positive forcings of the two scattering particle types (Figure 1).

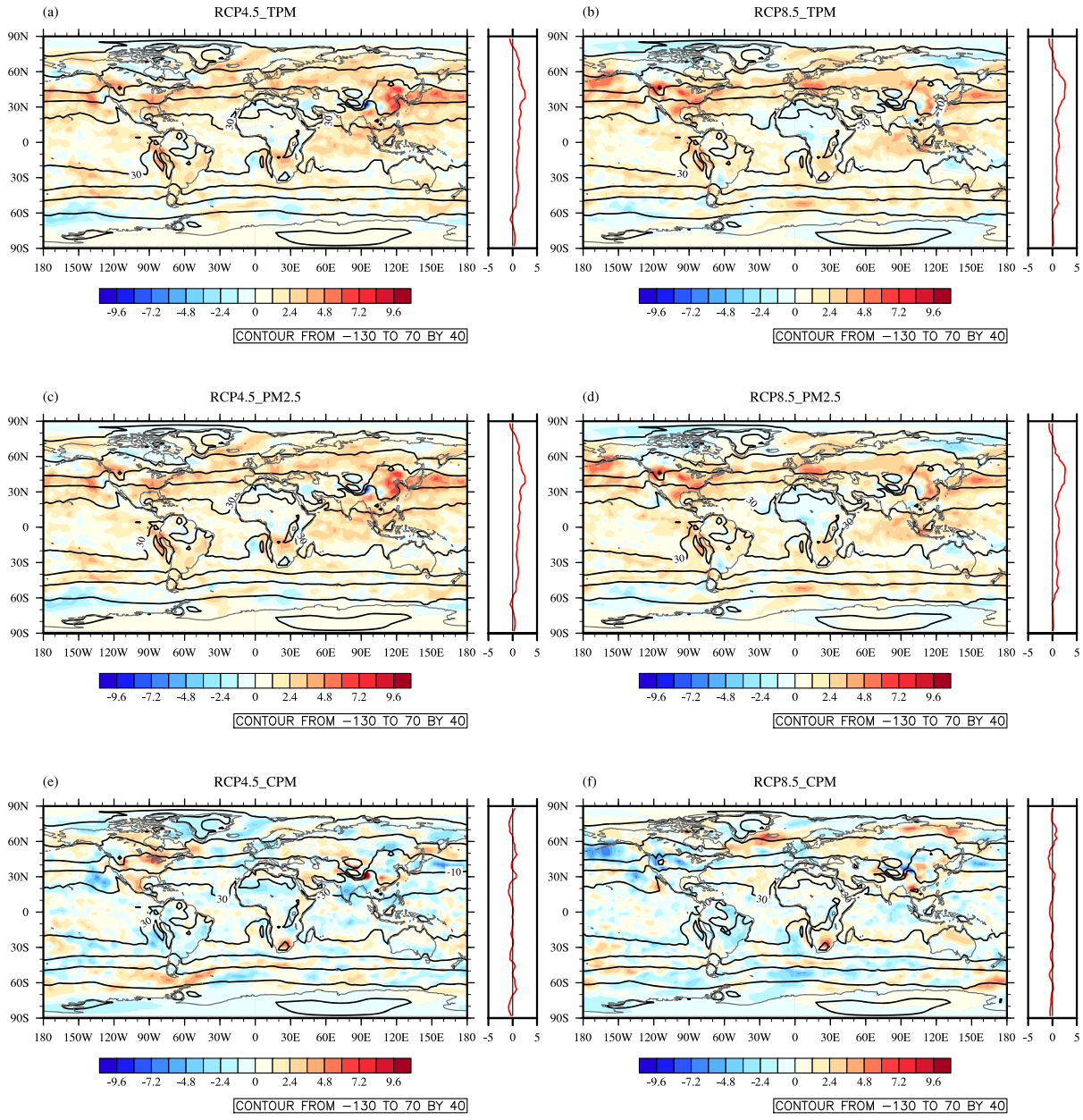


**Figure 3.** Color contours on the maps show changes in the spatial distributions of annual mean effective radiative forcing (ERF, relative to 2014; units: W $m^{-2}$), caused by changes in TPM (a, b), $PM_{2.5}$ (c, d), and CPM(e, f) burden under the RCP4.5 and RCP8.5 scenarios, respectively. Plots in the left column are simulated ERFs caused by changes in TPM, $PM_{2.5}$, and CPM under RCP4.5; plots in the right column are the same simulated ERFs under RCP8.5; the solid line contours show ERF in 2014; areas of ≥90% significance are plotted (areas that did not pass this criterion are shown in white).

For instance, relatively large increases in BC($PM_{2.5}$) occur in central Africa in both scenarios, but no apparent change in ERF occurs there. The increase in ERF due to BC($PM_{2.5}$) is offset by the decrease in ERF caused by increasing OC($PM_{2.5}$) over central Africa, whereas no significant changes in SF($PM_{2.5}$) particles are predicted over that region. Furthermore, the largest negative ERFs relative to 2014 occur over South Asia, reaching −12.04 W $m^{-2}$ under RCP4.5 and −10.41 W $m^{-2}$ under RCP8.5. Negative ERFs remain present over high-latitude areas in the NH, such as North America, mainly due to increased low cloud cover, which reflects more shortwave radiation (data not shown).

Global annual mean changes in ERF by CPM under the two scenarios are highly similar, that is, −0.06 W $m^{-2}$ for RCP4.5, and −0.07 W $m^{-2}$ for RCP8.5, but have the opposite sign to those due to $PM_{2.5}$. Based on scattering theory, small particles have stronger isotropic scattering and less absorption, resulting in more

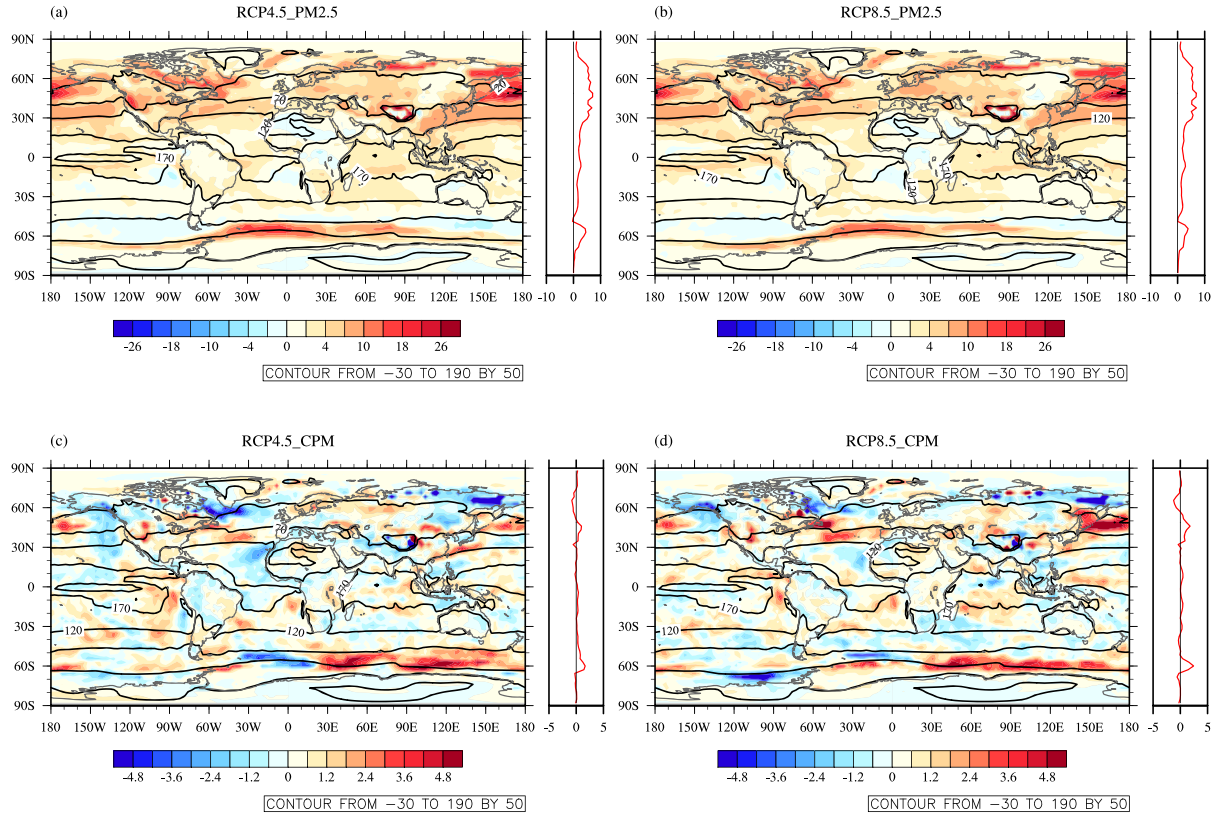


**Figure 4.** Color contours on the maps indicate the changes in the spatial distributions of annual mean surface net radiation flux (SNRF, Units: W $m^{-2}$) caused by changes in $PM_{2.5}$ (a, b) and CPM (c, d) burden under RCP4.5 and RCP8.5, respectively; plots in the left column are simulated results due to changes in $PM_{2.5}$ and CPM under RCP4.5, whereas plots in the right column are those under RCP8.5; the solid line contours show SNRF in 2014; areas of ≥90% significance are plotted (areas that did not pass this criterion are shown in white).

reflection at the TOA, whereas large particles have stronger forward scattering and absorption, resulting in less reflection at the TOA. Thus, small and large particles usually have opposite effects on radiative forcing, leading to very different ERFs due to $PM_{2.5}$ under different future aerosol scenarios. Aside from their opposite signs, the geographic distributions of changes in annual mean ERFs of CPM differ from those of $PM_{2.5}$ over many regions. The changes in ERFs due to CPM vary regionally. As Figures 1 and 2 show, the distributions of changes in $PM_{2.5}$ and CPM differ under both scenarios. The results for CPM contain more significant geographic variations than those of $PM_{2.5}$.

Although the global annual mean changes in ERFs due to changing CPM under the two scenarios are similar, their local distributions are different. For example, over North America, the ERFs under RCP4.5 are positive over the southern regions and negative over the northern regions, whereas negative ERFs are found over the whole area under RCP8.5. In addition, changes in ERFs over northern Asia under RCP8.5 are much stronger than those under RCP4.5, mainly due to differing changes in the absorbing particle burden over northern Asia under the two emissions scenarios.

### 3.2.2. Surface Net Radiative Forcing

ERF presented above shows the difference in net radiative flux at TOA from 2014 to 2050. Figure 4 shows the geographic distributions of changes in SNRF corresponding to aerosol emissions under RCP4.5 and RCP8.5 from 2014 to 2050. SNRF is equivalent to net radiative forcing at the surface, which is a crucial determinant of surface temperature change.

Global annual mean SNRF increase by 2.92 W $m^{-2}$ under RCP4.5, and 2.85 W $m^{-2}$ under RCP8.5, respectively, due to the reduction in anthropogenic $PM_{2.5}$ burden. These values are more than the double of the global annual mean ERFs by $PM_{2.5}$. Because most of the aerosols are located inside the atmospheric boundary layer, the impact on downward solar energy to the surface is much larger than on the reflected energy

to space. Reductions of aerosol under both RCP scenarios result in more solar energy reaching the surface. Since the surface albedo is usually close to 0.1–0.2, except for over snow and sea ice (Li et al., 2006), downward solar flux at the surface dominates SNRF. Thus, SNRF is a critical factor for changes in surface temperature (see discussion in Figure 6).

Under RCP4.5, the geographical distributions of changes in SNRF due to evolving $PM_{2.5}$ are very similar to those under RCP8.5. For both RCP scenarios, the values of SNRF due to changes in $PM_{2.5}$ increase significantly over most land and ocean areas, especially in the NH. Relative to 2014, the largest positive SNRFs are located over the northern Pacific Bering strait area, reaching 20 W $m^{-2}$ under both RCPs. However, this area does not show substantial reductions in $PM_{2.5}$, as presented in Figures 1 and 2. Therefore, SNRF changes are attributed mostly to climatic feedback. One feedback is from the cloud fraction change shown in Figure 10. Generally, increasing low and middle clouds fraction correspond to decreasing SNRF since low and middle clouds reduce surface solar irradiance. On the other hand, increasing high cloud fraction corresponds to increasing SNRF since high clouds attenuate outgoing longwave radiation and enhance SNRF. Over the lower and middle latitudes, changes in cloud fraction can explain much in the way of changes in SNRF. For example, over northern African for both scenarios where low cloud fractions change minimally and middle- and high cloud fractions decrease, resulting in a weak change in SNRF. Over tropical oceans west to African and South American, low and high cloud fractions increase and decrease, respectively, thereby enhancing SNRF. In the zonal band 25–50°N, both scenarios show decreases in low clouds over several large areas, with corresponding increases in SNRF.

In the polar jet stream region in the SH, large SNRF does not correspond to a considerable reduction of $PM_{2.5}$. for both scenarios. The increase in high cloud fraction in this area helps to explain why SNRF increases. However, the increase in low cloud fraction should produce opposite results. At high latitudes, changes in sea ice extent can affect SNRF as well. This is because reduced sea ice can decrease surface albedo, thus increases the SNRF.

Meanwhile, these values increase by 0.19 W $m^{-2}$ under RCP4.5, and 0.23 W $m^{-2}$ under RCP8.5, respectively, due to changes in CPM burden. These values are also much larger than the corresponding results of ERF. As with ERF, the signs of SNRF for $PM_{2.5}$ and CPM are opposite in most areas. Moreover, the geographic distributions of changes in annual mean SNRFs of CPM significantly differ from those of $PM_{2.5}$. The same for SNRF due to $PM_{2.5}$, region of large reductions in the CPM loading are generally not associated with significant increases in SNRF. For example, while there is a large SNRF due to CPM in the polar stream region in the SH, but there is no response from changes in CPM loading.Similar to PM2.5, the results of SNRF due to CPM are also associated with the changes of cloud and sea ice (detailed analysis neglected).

#### 3.2.3. Energy Transport

Apart from the radiative flux, poleward energy transport (PET) due to decreases in $PM_{2.5}$ burden is also a key diagnostic factor, which could help to analyze the warming pattern shown in the next section. Huang et al. (2017) showed that energy transportation could be indicated directly from changes in PET. According to Huang et al. (2017),

$$PET(\phi) = 2\pi a^2 \int_{-\pi/2}^{\phi} (R(\phi') - \bar{R})cos(\phi')\, d\phi' \tag{1}$$

where $PET(\phi)$ is the northward energy flux across the latitude $\phi$, $R(\phi)$ is the zonal mean net radiation flux at latitude $\phi$, and $\bar{R}$ is the global mean net radiation flux; $a$ is the radius of the Earth. Changes in PET at TOA, surface, and atmosphere due to anthropogenic $PM_{2.5}$ and CPM are shown in Figure 5. For fine particles, PET at TOA and surface decreases in the SH and increase in the NH under both RCP4.5 and RCP8.5. The maximum negative PET at TOA and surface occurs over regions near 30°N. Because the results are the anomalies to the global mean, the regions of negative curve slope correspond to the accumulated negative anomaly, as the values of $R(\phi)$ are smaller than the global mean of $\bar{R}$. In the positive slope regions, the anomalies become positive. Therefore, the results of PET at TOA and surface indicate that the warming effect is more apparent in the NH than SH. The atmospheric PET due to fine particles is the difference between the results of TOA and surface. Atmospheric PETs are positive because the results of PET at the surface is much more negative than those at TOA. Results of PET are similar to those of doubling $CO_2$ shown in Huang et al. (2017), because it could result in surface warming in both cases. The enhancement of atmospheric PET, accompanied by the weakening of oceanic PET are shown in Figure 5, which indicates that the energy is transported from low- to high-latitude regions, especially in the NH (Huang et al., 2017; Hwang & Frierson,

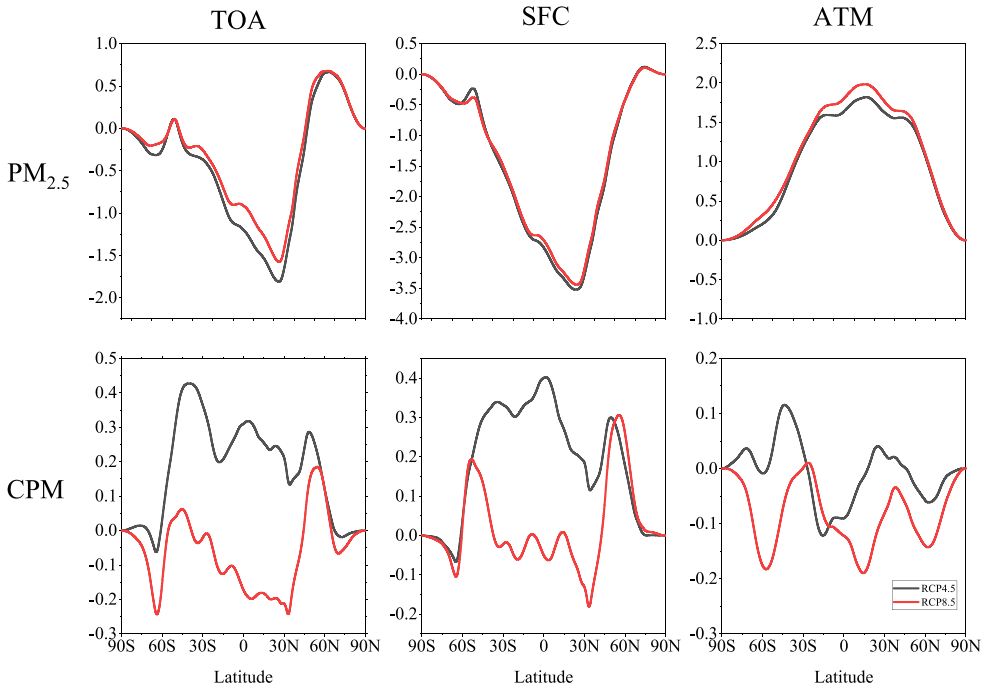


**Figure 5.** Changes in TOA, surface (SFC), and atmospheric (ATM) PET (units: 1,014 W $m^{-2}$) caused by $PM_{2.5}$ and CPM from 2014 to 2050 under the RCP4.5 and RCP8.5, respectively. Shown in different rows are changes due to varied column concentrations of $PM_{2.5}$ and CPM under different scenarios, respectively. Results from the RCP4.5 scenario are shown in black, and from the RCP8.5 scenario are shown in red.

2010). Changes of PET at TOA, surface, and atmosphere caused by varied CPM from the year 2014 to 2050 are almost opposite to those of $PM_{2.5}$. This is consistent with the different distributions of TOA, surface, and atmospheric net radiation flux due to CPM under the two emissions scenarios.

### 3.3. Climatic Effects

Sensitivity experiments for the climate response to changes in anthropogenic $PM_{2.5}$ and CPM are described in section 2. We considered two climate states, that is, driven by TPM and $PM_{2.5}$; the difference between these two simulations for each year is defined as the state of CPM. The climate state driven only by $PM_{2.5}$ has been discussed previously (Fu et al., 2016); it is theoretical, as the whole aerosol size spectrum is always present. However, the comparison between the model states based on $PM_{2.5}$ and CPM can illustrate the role played by $PM_{2.5}$ in future climate change. If the results based on $PM_{2.5}$ and CPM show opposite signs in a climate signal or pattern, $PM_{2.5}$ has a stronger influence than TPM on climate, and vice versa. Therefore, future climates driven by $PM_{2.5}$ and CPM can help illuminate the quantitative and systematic relationships between anthropogenic aerosols and climate change.

#### 3.3.1. Surface Air Temperature

Figure 6 shows the geographic distributions of changes in surface air temperature (SAT) under RCP4.5 and RCP8.5 from 2014 to 2050. Global annual mean SAT increases by 1.25 K under RCP4.5, and 1.22 K under RCP8.5, respectively. Geographic distributions of the changes in SAT due to anthropogenic $PM_{2.5}$ are also very similar under RCP4.5 and RCP8.5, due to similar reductions in fine particle emissions under the two scenarios. The reduction in $PM_{2.5}$ concentrations leads to a worldwide warming, especially over the NH land and oceanic regions at middle and high latitudes, contributing significantly to future global warming. This warming effect is more apparent over high-latitude regions, with the greatest increases in SAT of 5.23 K under RCP4.5 and 5.04 K under RCP8.5 over the northern Pacific Ocean, mainly due to the reduced scattering effects of fine SF($PM_{2.5}$) and OC($PM_{2.5}$) particles under future emissions scenarios. Slight increases in SAT occur at high latitudes of the SH due to small changes in fine particles, caused in part by decreases in sea ice due to climate feedback, weakening the reflection of solar radiation (data not shown).

Changes in SAT are, to some extent, related to changes in ERF, as ERF measures the trapping or loss of radiative energy in the atmosphere by the perturbed anthropogenic aerosol concentration. As shown in

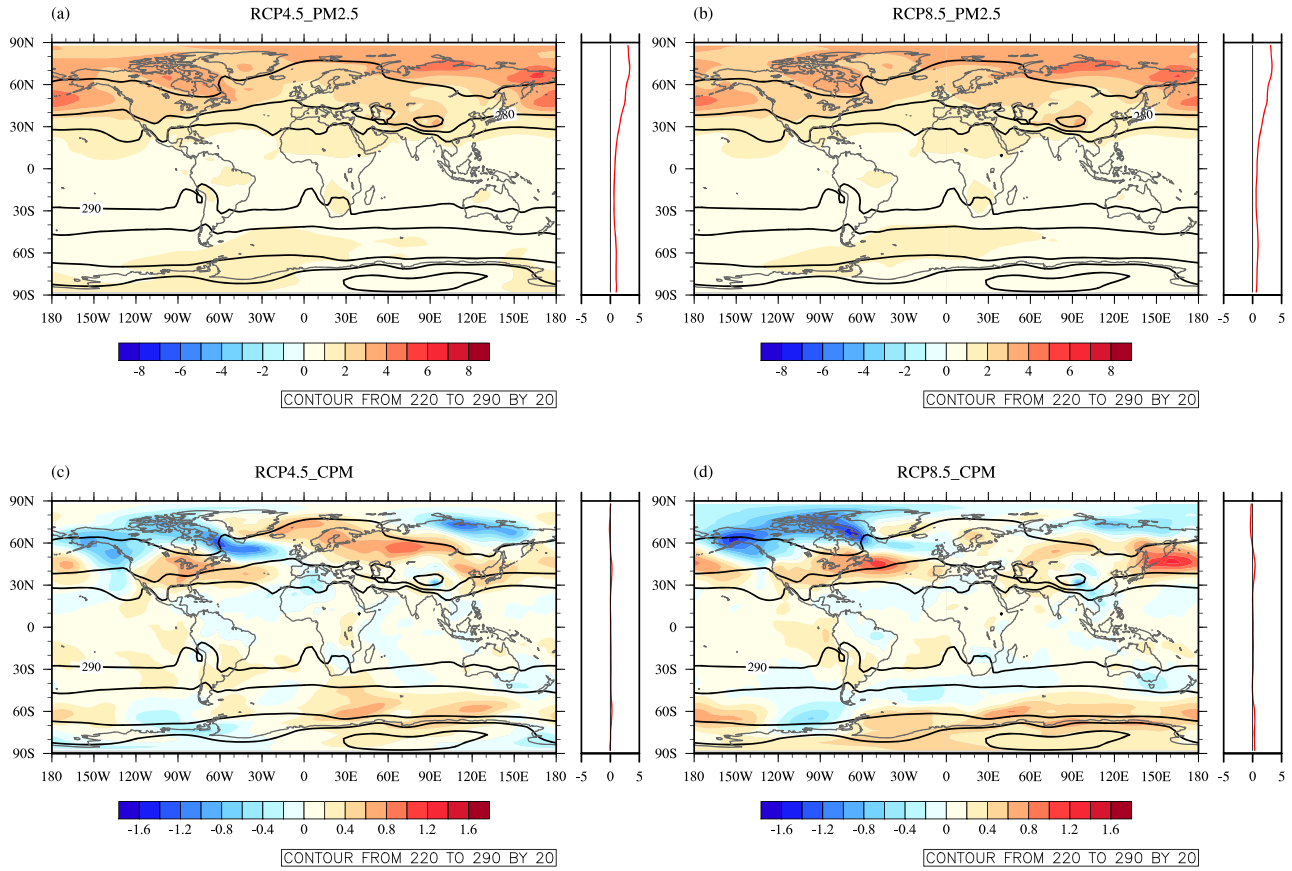


**Figure 6.** Color contours on the maps indicate the changes in the spatial distributions of annual mean surface air temperature (SAT, units: K) caused by changes in $PM_{2.5}$ (a, b) and CPM (c, d) burden under RCP4.5 and RCP8.5, respectively; plots in the left column are simulated results due to changes in $PM_{2.5}$ and CPM under RCP4.5, whereas plots in the right column are those under RCP8.5; the solid line contours show SAT in 2014; areas of ≥90% significance are plotted (areas that did not pass this criterion are shown in white).

Figures 3 and 6, both of the changes of ERF and SAT due to $PM_{2.5}$ are generally positive in the NH. However, the local correlation between the two physical quantities is weak because the change in energy at TOA does not directly influence the surface. Instead, changes in SAT are related strongly to changes in SNRF. Over most land areas, especially in the NH, Figures 4 and 6 show that changes in SNRF are generally consistent with those of SAT. For example, over the northern Pacific Bering strait area, both SNRF and SAT exhibit the maximum changes due to reduction of $PM_{2.5}$. The same correlation between SNRF and SAT can be found over high-latitude regions as well. For example, in the polar jet stream region near 60°S, both SAT and SNRF increase. However, significant differences between SAT and SNRF occur over the Arctic region, where an increase in SAT corresponds weakly to the change in SNRF. Since incoming solar energy decreases with latitude, SNRF becomes very weak in polar regions (Li, 2017). Thus, we do not expect a physical explanation for changes in SAT based on SNRF. There must be other factors. Figure 5 shows energy transport from low to high latitudes mainly through the atmosphere, to be associated with the hydrological cycle and general circulation, respectively (Huang et al., 2017). An increase in atmospheric PET, along with negative surface PET (shown in Figure 5) are noticeable climatic responses during global warming (Hwang & Frierson, 2010). Though energy transports from low to high latitudes occur in both hemispheres, the curve of atmospheric PET shown in Figure 5 strongly tilts toward the Arctic, meaning that much more energy is transported to high latitudes in the NH than in the SH (this is supported by the results of Hadley circulation showing below). Therefore, positive atmospheric PET is a critical factor for warming in the Arctic. Changes in the atmospheric circulation shown in the following section will illustrate in more detail the energy transport to high latitudes in the NH.

The global annual mean SAT increases by 0.10 K under RCP4.5, and 0.10 K under RCP8.5, respectively, due to changes in CPM burden. Changes in SAT caused by CPM are about one order of magnitude smaller than

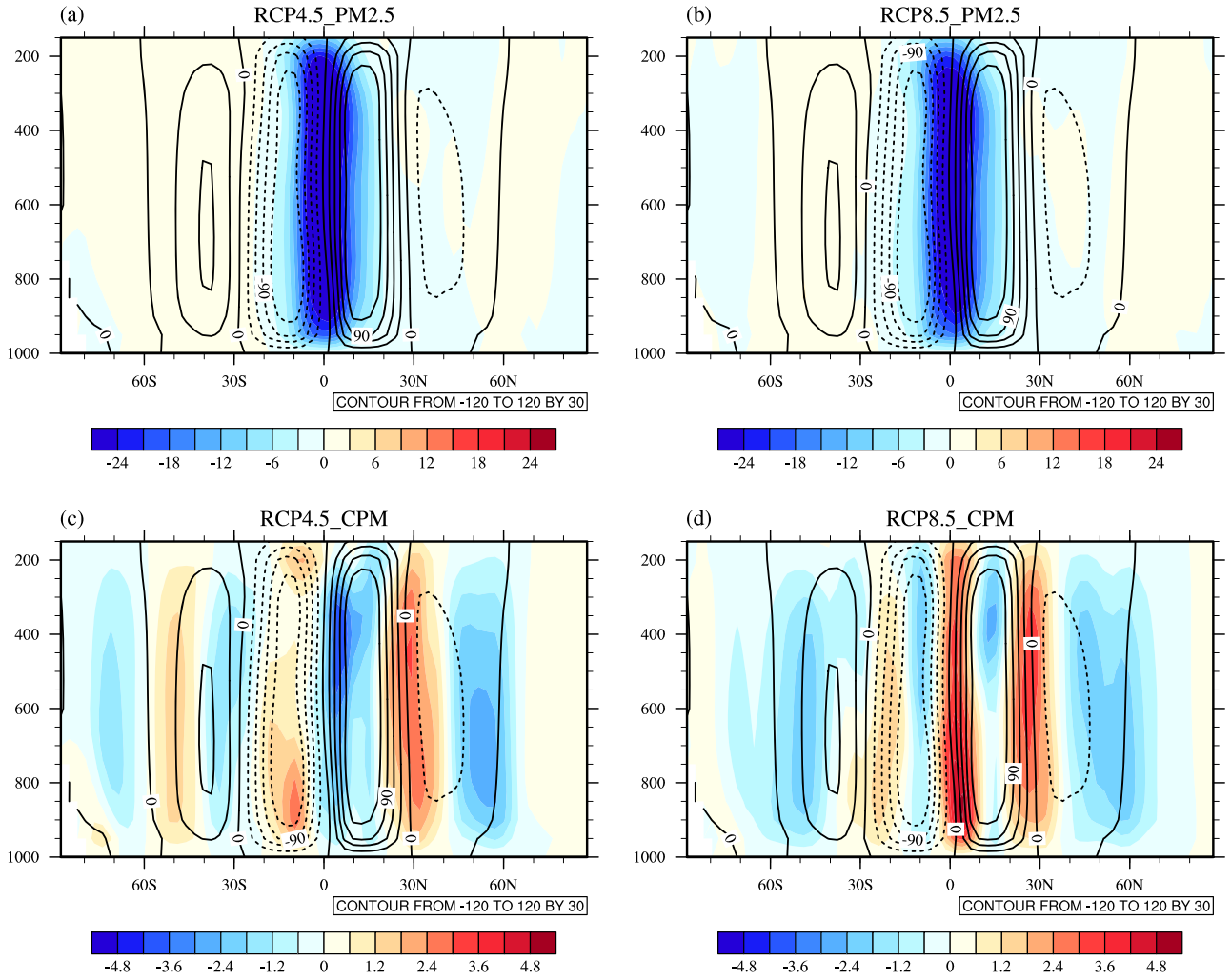


**Figure 7.** Color contours in the maps show changes in stream function of vertical atmospheric circulation (Units: $10^{-11}$ kg $s^{-1}$) caused by changes in $PM_{2.5}$ and CPM burden under the RCP4.5 and RCP8.5 scenarios; panels (a) and (c) are simulated results caused by changes in $PM_{2.5}$ and CPM under RCP4.5, whereas panels (b) and (d) are those under RCP8.5; the solid line contours in (a)–(d) show the stream function of vertical atmospheric circulation in 2014; the areas of ≥90% significance are plotted (areas did not pass this criterion are shown in white).

those due to changes in $PM_{2.5}$. Unlike the orderly patterns observed in the distribution of changes in SAT due to $PM_{2.5}$, changes in SAT due to the CPM burden from 2014 to 2050 are less clearly patterned, with both positive and negative values predicted. There are obvious correlations between the changes in SAT and SNRF due to CPM. For example, at high latitudes over North America, simulated SATs caused by the changes in CPM decrease notably under RCP4.5, with a maximum reduction of 0.90 K; even stronger decreases occur under RCP8.5, with a reduction of 1.30 K. The significant decreases of SNRF are also found in this area.

Furthermore, many local areas, show increases in annual mean SATs due to changes in CPM, especially in regions near 40°N and 70°S. Over southern North America, northern Europe, northwest Asia, and their neighboring oceanic regions, distinct increases in SATs are found under RCP4.5, whereas the most distinct changes in SATs occur over northern Europe and northwest Asia under RCP8.5. In general, these regions correspond to the positive values of SNRF. Changes in SATs are smaller over the tropics in both hemispheres. Changes in SATs in response to $PM_{2.5}$ and CPM are more significant over high-latitude regions in the NH. One reason for this pattern is that the temperature at high latitudes is more sensitive to external disturbances (Zhang et al., 2016; Zhou et al., 2017).

### 3.3.2. Atmospheric Circulation

Changes in atmospheric temperature under the two RCP scenarios, shown in Figure 6, could influence energy transport between the two hemispheres, which could in turn affect atmospheric circulation. Figures 7

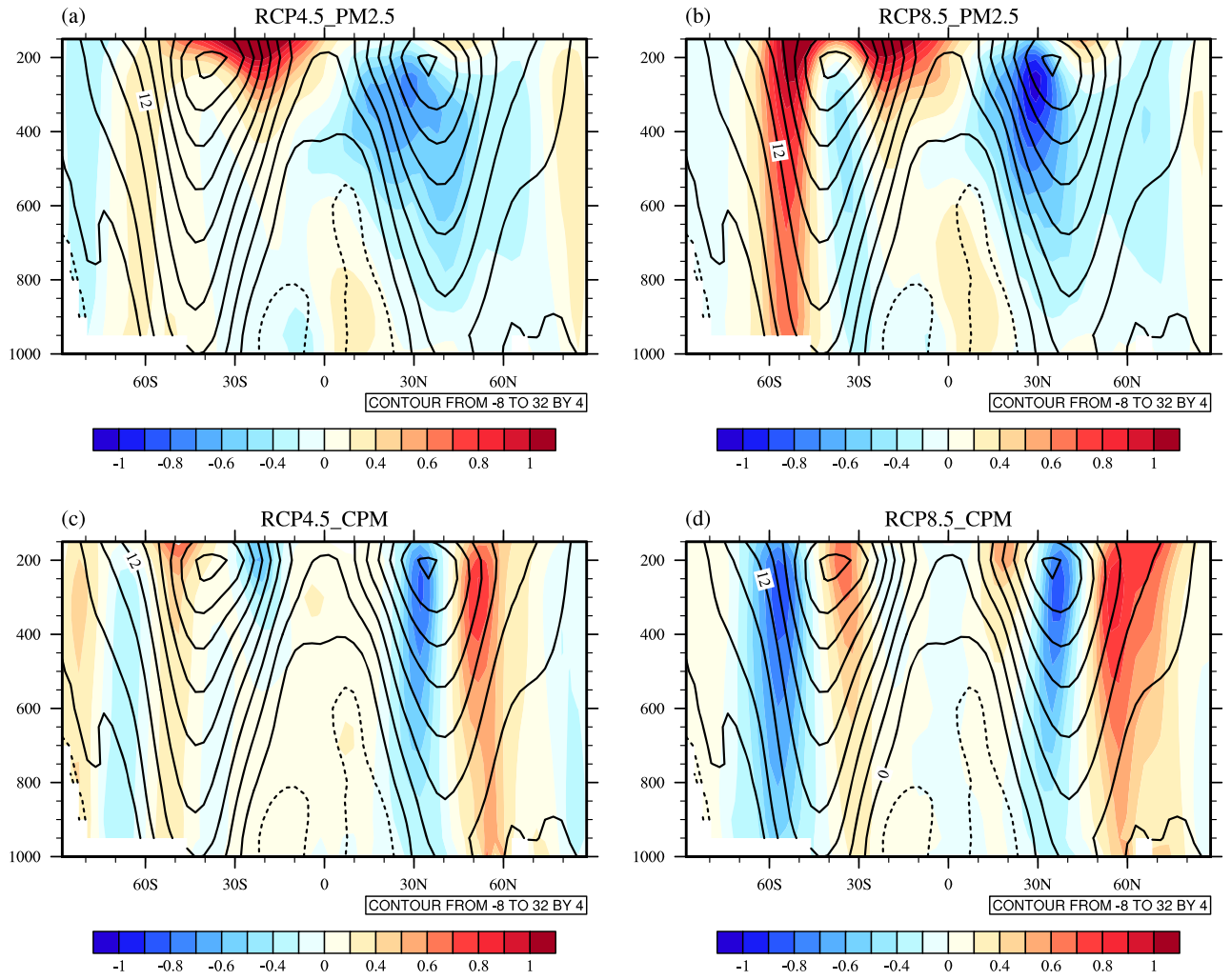


**Figure 8.** As described in Figure 7 but showing changes in the spatial distributions of annual mean averaged zonal wind (units: m $s^{-1}$) caused by changes in $PM_{2.5}$ and CPM burden under RCP4.5 and RCP8.5.

and 8 show atmospheric stream function and the vertical distribution of zonal mean U wind velocity in 2014 along with and the corresponding changes due to $PM_{2.5}$ and CPM from 2014 to 2050 under RCP4.5 and RCP8.5. Changes in atmospheric circulation are essential information for determining the differing climatic effects of fine and coarse particles under future emissions scenarios.

Changes in stream function due to decreased $PM_{2.5}$ under the RCP4.5 scenario are found very similar to that under RCP8.5 (Figures 7a and 7b). The increase in SAT toward the polar region in the NH indicates a temperature gradient decreasing northward, which weakens the Hadley cell in the NH. This causes the Hadley cell in the NH to move northward, as evidenced by the equatorial anomalies of Hadley circulation over 10°S 1°0N. The Ferrel cell is also weakened in the NH under both emissions scenarios. In the SH, the SAT gradient decreases toward the polar region, leading to a strengthened Hadley cell that can modulate the westerly jet streams, with intensive descending branches of circulation weakening of the subtropical jet near 30°S due to Coriolis force (Figures 7c and 7d). The enhanced Hadley circulation in SH and northward meridional cells, result in the energy transported to the Arctic region, which is consistent with the warming pattern in Figure 6. In the SH, the Ferrel cell is also enhanced slightly under both RCP4.5 and RCP8.5, which could cause increases in the westerlies over oceanic regions near 60°S. Strengthened westerly jet streams are more apparent under the RCP8.5 scenario (Figure 7d). The accelerated baroclinicity caused by changing temperature distributions could have impacts on the jet stream. Additionally, the northward ascending branches of the Hadley could cause a shift of the ITCZ in the same direction, which could affect

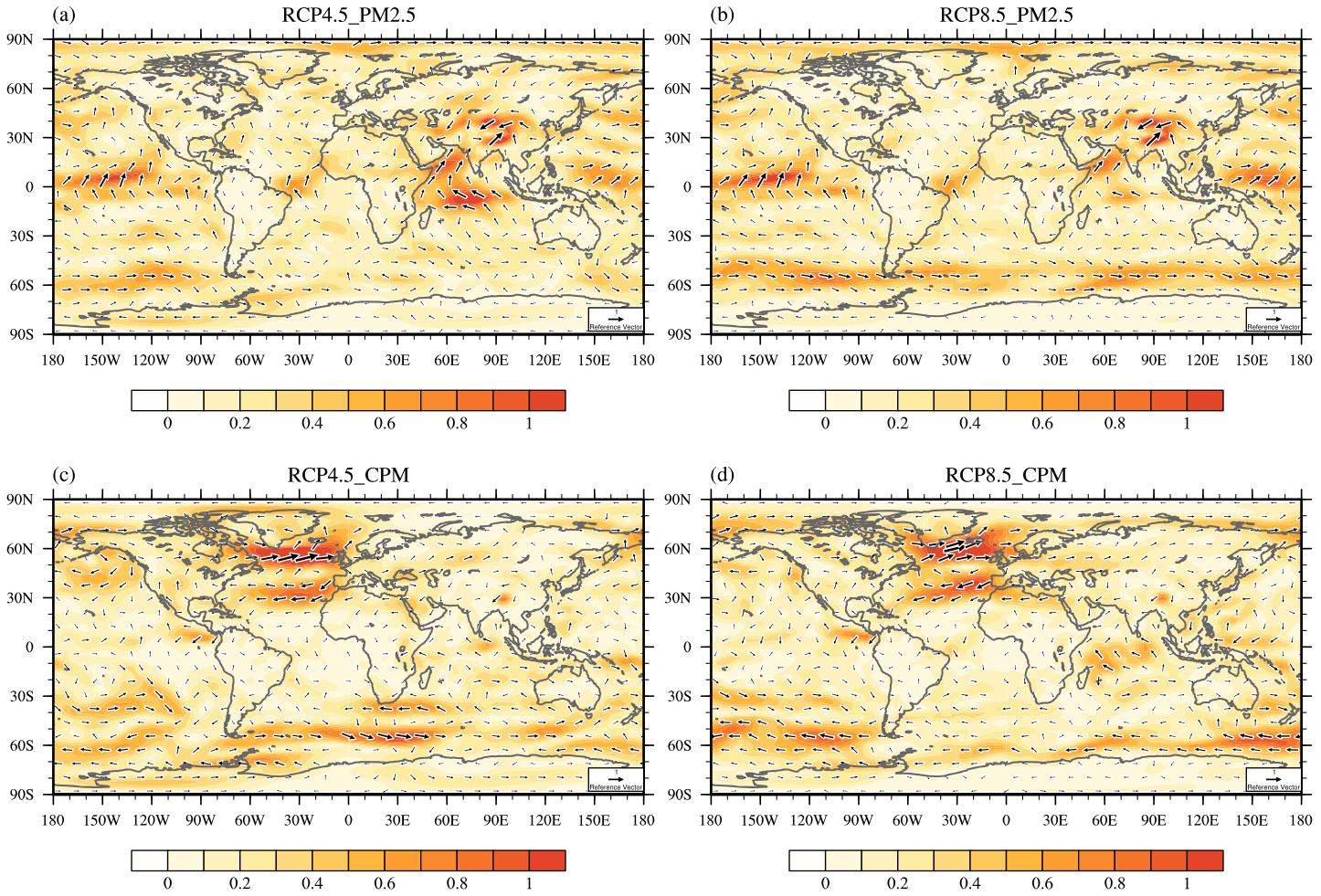


**Figure 9.** Changes in surface horizontal wind (shaded areas represent the wind speed; units: m $s^{-1}$) caused by changes in $PM_{2.5}$ (a, b) and CPM (c, d) burden under the RCP4.5 and RCP8.5 scenarios; plots in the left column are simulated results caused by changes in $PM_{2.5}$ and CPM under RCP4.5, whereas plots in the right column are simulated under RCP8.5.

the precipitation patterns in the tropics. Furthermore, changes in the strength of the descending branches of Hadley cells in both the NH and SH, would lead to changes in the distribution and intensity of precipitation over low- and middle-latitude regions. This possibility will be discussed in detail in the following section.

Figures 7c and 7d show changes in the stream functions of vertical atmospheric circulation due to the changing CPM column concentrations between 2014 and 2050 under RCP4.5 and RCP8.5. Changes in stream functions due to CPM are distinct from those due to $PM_{2.5}$, as they are nearly one order of magnitude smaller. Under the RCP4.5 scenario, the Hadley cells are weakened in both hemispheres, mainly due to the geographic distributions of changing SAT due to coarse particles. However, under the RCP8.5 scenario, the Hadley cell in the NH is strengthened and that in the SH is weakened. The Hadley cells are also influenced by the changing distributions of atmospheric temperature due to CPM (see Figure 6). Compared to the results of RCP4.5, the westerly polar jet streams are enhanced in the NH, and weakened in the SH under RCP8.5, along with changes in atmospheric circulation (Figure 7h). Given that the climate state due to CPM is the state due to TMP minus that due to $PM_{2.5}$, $PM_{2.5}$ could have a larger (smaller) impact on climate compared to total aerosols, if the effects of CPM are positive (negative) compared to those of $PM_{2.5}$.

We denote the zonal and meridional surface wind speeds as $U$, and $V$, respectively. Figure 9 shows changes in the surface horizontal wind vectors ($U$, $V$) and the absolute wind speed (shading) due to changing $PM_{2.5}$ and CPM from 2014 to 2050, under RCP4.5 and RCP8.5. Like other climatic variables, changes in the surface horizontal wind vector due to the reduction of $PM_{2.5}$ are very similar under RCP4.5 and RCP8.5 (Figures 9a and 9c). Enhancement of surface wind vectors from ocean to land is predicted over East Asia, as is the

cross-equatorial flow over the Indian Ocean; these results are consistent with those of previous studies (Wang, Lin, et al. 2017; Wang, Wang, et al. 2017). Northeasterly trade winds over the tropics in the NH weaken markedly, especially over the central Pacific Ocean and the Indian Ocean, due to the weakness of the NH Hadley cell. The Eastward zonal winds over oceanic regions near 50°S strengthen due to the enhanced Hadley cell in the SH. For changes in wind vectors due to varied CPM particles, those of surface winds under RCP4.5, are distinct from those under RCP8.5; this difference is linked to changes in the Ferrel cells of both the SH and NH, as shown in Figure 7.

#### 3.3.3. Clouds and Precipitation

Figure 10 shows changes in low cloud cover (above 680 hPa), middle cloud cover (between 440 and 680 hPa), high cloud cover (below 440 hPa), and total cloud cover (TCC; sum of the low, middle, and high cloud fractions) due to changes in fine particles, and changes in TCC caused by coarse particles under RCP4.5 and RCP8.5 from 2014 to 2050. Simulated global annual mean TCC increases by 0.02% under both RCP4.5 and RCP8.5 due to changes in $PM_{2.5}$, whereas TCC decreases by 0.08% under RCP4.5 and increases by 0.11% under RCP8.5 due to CPM changes. Although changes in global annual mean TCC due to changing $PM_{2.5}$ and CPM are very small, regional cloud changes are much more significant, with different trends and distributions of changes in the cloud fraction between the fine and coarse particles.

Due to the decrease in $PM_{2.5}$, large increases in annual mean TCC are predicted over vast areas at high latitudes in the NH, with maximum increases of 11.42% under RCP4.5 and 11.72% under RCP8.5. Clouds can shade the solar energy from reaching the surface, thereby causing a cooling effect. However, this is not true in the high latitudes of NH and Arctic, where the increase of TCC corresponds to the enhancement of SAT. As mentioned above, the incoming solar energy is very weak in these regions, which is not the dominant factor for the warming effect. Additionally, significant increases occur at high latitudes of the SH. The significant increases in TCC predicted at high latitudes of the NH agree well with the corresponding changes in SAT, as shown in Figure 6. Over high-latitude and polar regions, longwave radiation is more important than solar radiation. Increased cloud cover in these regions can reduce outgoing longwave radiation and warm the surface (Figures 6 and 10). Slight increases in the TCC are observed over 10N in the tropics, mainly due to strengthening of the northward ascending branches of the Hadley cell in the NH. In contrast, simulated annual mean TCC decreases significantly over land and oceanic regions near 30°N, as well as lower-latitude regions of the SH. This decrease in TCC is caused by enhancement of descending branches of the Hadley cells in both hemispheres. The region of decrease is broader in the SH than in the NH, mainly due to the strengthened Hadley cell in the SH, with enhanced descending branches.

Figure 10 shows variations of annual mean TCC due to changes in CPM burden under both RCP scenarios from 2014 to 2050. The geographic distributions of changes in the cloud fraction are more irregular than those due to $PM_{2.5}$, with a much smaller maximum increase in TCC than that due to $PM_{2.5}$. This irregular pattern is associated with irregular changes in CPM column concentrations, atmospheric circulation, and climate feedbacks. Figure 11 shows changes in precipitation due to changes in $PM_{2.5}$ and CPM burden under RCP4.5 and RCP8.5 from 2014 to 2050. Due to the reduction in $PM_{2.5}$, global annual mean precipitation increases by 0.10 mm $day^{-1}$ by 2050 under both RCP4.5 and RCP8.5. The geographic distributions of changes in precipitation under RCP4.5 are very similar to those under RCP8.5. Precipitation increases over regions near 10N in the NH tropics but decreases over regions near 10S in the SH tropics (Figures 11a and 11c). These patterns of change in precipitation are mainly caused by the northward shift of the ITCZ and by the northward movement of ascending branches of Hadley circulation due to $PM_{2.5}$ reduction, as shown in Figure 11. The geographic distributions of changes in precipitation are correlated with those of changes in TCC (Figures 10 and 11). Moreover, precipitation is found to increase in middle- and high-latitude regions of both hemispheres, along with rising TCC over these regions. Generally, the distributions of changes in precipitation over the tropics are consistent with those of TCC due to the decreases in $PM_{2.5}$ column concentrations in the future. Moreover, as mentioned above, the atmospheric PET caused by $PM_{2.5}$ is negative in the NH, with an extra cooling atmosphere near the equator, leading to the increases in precipitation (Figures 6 and 10).

For CPM, changes in precipitation are much smaller than those associated with $PM_{2.5}$, with global annual mean precipitation increasing by 0.01 mm $day^{-1}$ under both RCP scenarios. Apparent increases and decreases in precipitation due to changes in CPM occur over the tropics, as observed for $PM_{2.5}$. However, the signs of changes in precipitation caused by varied CPM are opposite to those caused by decreased $PM_{2.5}$ over most regions, especially Asia, North America, South America, the Indian Subcontinent, and the Pacific

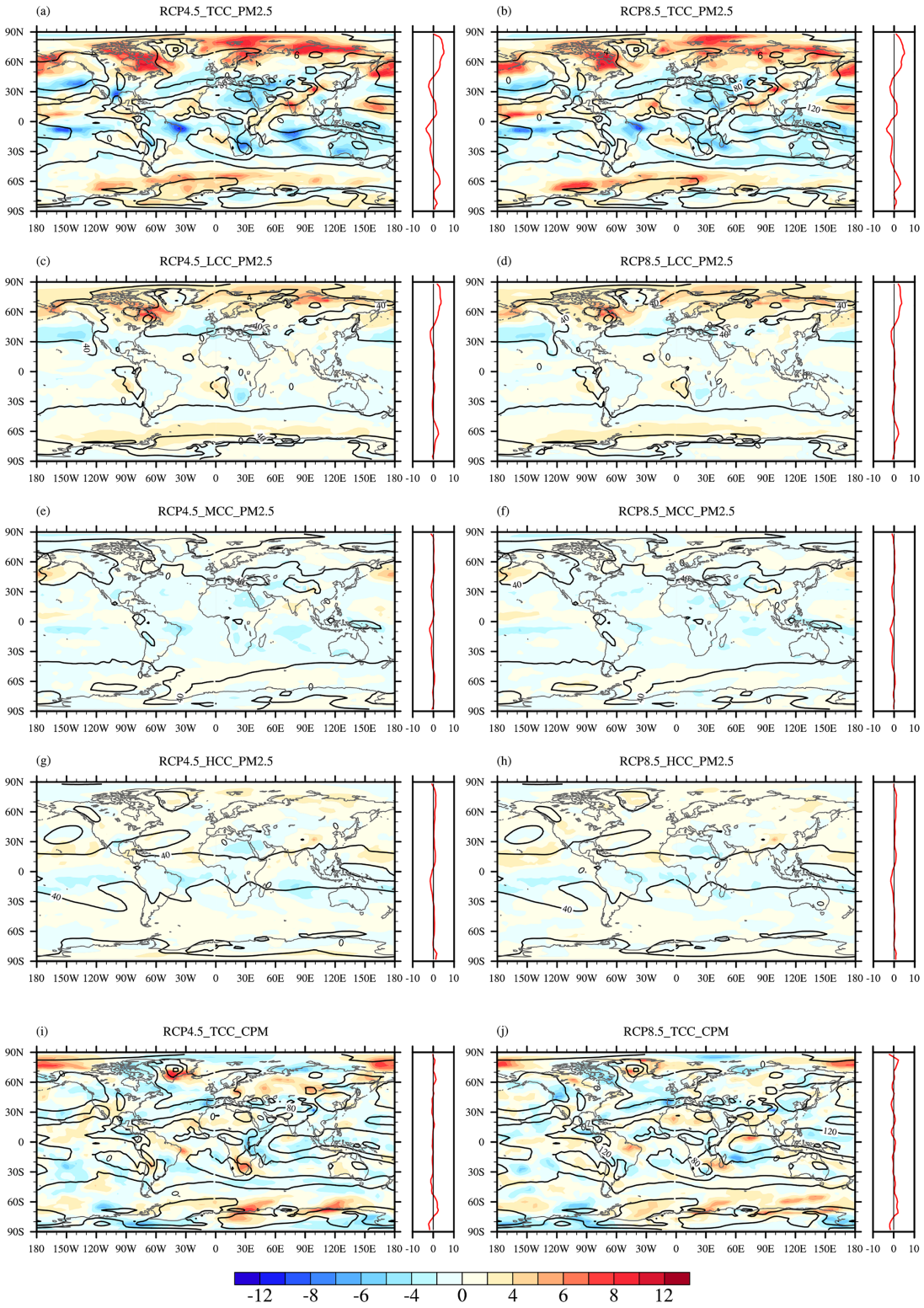


**Figure 10.** Color contours on the maps show the changes in the spatial distributions of annual mean total cloud fraction (a, b) (TCC; units: %), low cloud fraction (c, d) (LCC; unit: %), middle cloud fraction (c, d) (LCC; unit: %), and high cloud fraction (e, f) (HCC; unit: %) caused by changes in $PM_{2.5}$ burden and total cloud fraction (a, b) (TCC, Unit: %) caused by changes in CPM (g, h) burden under the RCP4.5 and RCP8.5 scenarios, respectively; plots in the left column show simulated results caused due to changes in $PM_{2.5}$ and CPM under RCP4.5, whereas plots in the right column show those under RCP8.5; the solid line contours show TCC in 2014; the areas of ≥90% significance are plotted (areas that did not meet this criterion are shown in white).

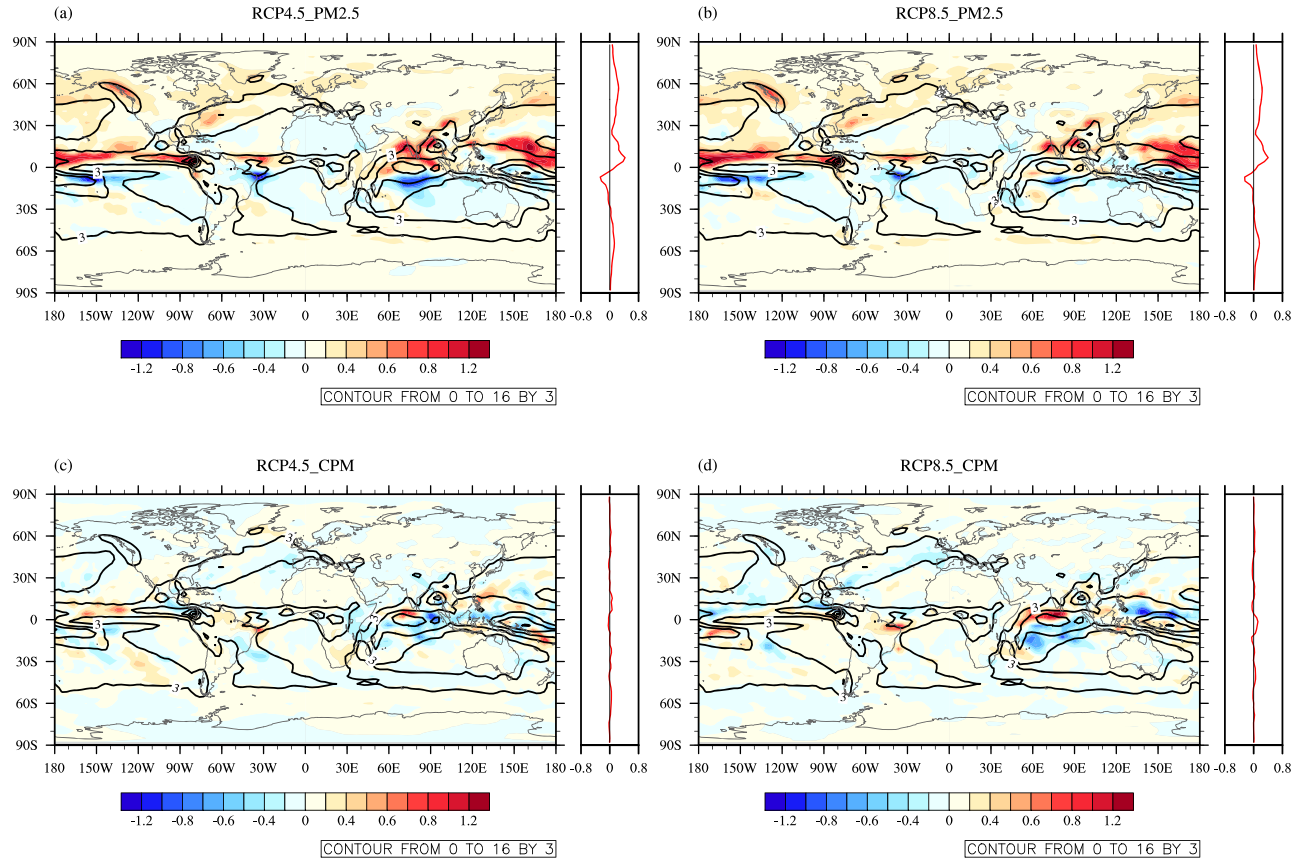


**Figure 11.** As described in Figure 10 but showing changes in the spatial distributions of annual mean precipitation (Units: mm day$^{-1}$) caused by changes in $PM_{2.5}$ and CPM burden under the RCP4.5 and RCP8.5.

Ocean. Simulations show that particles of different sizes could result in different changes in global precipitation under RCP4.5 and RCP8.5. The global annual mean values and geographic distributions of changes in precipitation caused by $PM_{2.5}$ (CPM) are similar under both scenarios. Thus, we conclude that the reductions in $PM_{2.5}$ (CPM) makes little differences in their impact on global climate through 2050 under both RCP scenarios, supporting recommendations to implement the emission reduction strategies in the future.

## 4. Conclusions

Anthropogenic aerosols are the most important type of air pollutants, and much government effort has been devoted to constraining their continuous growth. Under future climate scenarios, the emissions of anthropogenic aerosol are assumed to decrease. Using the aerosolclimate coupled model BCC_AGCM2.0_CUACE/Aero, we explored the impacts on radiative forcing and climate due to reductions in emissions of anthropogenic aerosols under future scenarios RCP4.5 and RCP8.5 during from to 2050. Aside from anthropogenic aerosol emission data of RCPs, updated emissions data for particles in 2014 obtained from Community Emissions Database System were used, which are regarded as closer to actual particle emissions (Hoesly et al., 2018). The aerosol size distribution was considered by addressing the individual roles of $PM_{2.5}$ and CPM. The following conclusions could be drawn from the research discussed.

Changes in anthropogenic $PM_{2.5}$ burden dominate the total changes in TPM from 2014 to 2050, and $PM_{2.5}$ loads decrease over most continental interiors, especially East Asia, under both RCP4.5 and RCP8.5. In contrast to $PM_{2.5}$, CPM column concentrations vary among regions. The CPM burden increases over northern Asia, North America, and central Africa but decreases over most regions of East Asia and North Africa. The different life spans of $PM_{2.5}$ and CPM lead to differences in the dynamics of their burdens. Relative to 2014, changes in ERFs due to changing $PM_{2.5}$ are positive over most land and oceanic regions. Negative forcing associated with CPM is mainly due to increases in SF(CPM). Warming caused by $PM_{2.5}$ occurs over most

areas of land and ocean, especially in high latitudes of the NH, whereas changes in SAT due to CPM are negative over high latitudes of North America and North Asia. Changes in SAT are highly correlated with those of SNRF, a critical factor affecting global SAT. The Hadley cell in the NH weakens and moves northward, whereas the corresponding circulation in the SH strengthens. Meanwhile, the ITCZ rain center shifts to near 10N, mainly due to the asymmetry of atmospheric temperature between the NH and SH induced by the radiative effects of $PM_{2.5}$. Precipitation is predicted to increase (decrease) over tropical regions of the NH (SH). Changes in atmospheric circulation by changing CPM differ greatly from those due to changing $PM_{2.5}$. Precipitation variations over the tropics are associated with changes in the cloud fraction for both $PM_{2.5}$ and CPM.

Anthropogenic $PM_{2.5}$ contributes significantly to future climate change, and CPM often plays the opposite role. If the results due to $PM_{2.5}$ and CPM show the opposite signs in climate signals or patterns, $PM_{2.5}$ is stronger than TPM in influencing climate, whereas TPM is stronger if their signs are the same. Moreover, reductions in fine particles, especially SF particles, could aggravate global warming in the future, whereas reductions in coarse particles play a weaker role in warming.

Please note that the nitrate and secondary OC aerosols are not included in the aerosolclimate coupled model used in this research, which may lead to some underestimation of the simulated results (Wang et al., 2010; Zhu et al., 2017). A new version of this aerosolclimate online model with nitrate and secondary OC aerosols is being tested, and it can improve the simulations of radiative and climatic effects more appropriately in the future. Furthermore, the coarse horizontal resolution used in this study might not fully resolve the aerosol climate effect. These aspects could be improved or even avoided by updating the coupled model. Aside from these two limitations, our research on the climate response provides a meaningful quantitative assessment of the climate impacts by $PM_{2.5}$ under future emissions scenarios.

**Acknowledgments**
Emissions of anthropogenic aerosol particles and their precursors in 2014 were determined from Community Emissions Database System (CEDS), a data set that provides a gridded historical inventory of climate-related anthropogenic aerosols for use in CMIP6 (Hoesly et al., 2018). Emissions of aerosol particles and their precursors in 2050 were obtained from the IPCC RCP Database (Clarke et al., 2007; Riahi et al., 2007; Smith & Wigley, 2006; Wise et al., 2009). This work is financially supported by the (Key) National Natural Science Foundation of China (Grants 91644211 and 41575002) and National Key R&D Program of China (Grant 2017YFA0603502). D. Y. acknowledged the financial aid from China Scholarship Council (Grant 201808320289) to visit Canadian Center for Climate Modeling and Analysis.

## References

Bollasina, M. A., Ming, Y., & Ramaswamy, V. (2011). Anthropogenic aerosols and the weakening of the south Asian summer monsoon. *Science*, *334*(6055), 502–505.

Bond, T. C., Doherty, S. J., Fahey, D., Forster, P., Berntsen, T., DeAngelo, B., et al. (2013). Bounding the role of black carbon in the climate system: A scientific assessment. *Journal of Geophysical Research: Atmospheres*, *118*, 5380–5552. https://doi.org/10.1002/jgrd.50171

Chiang, J. C., & Friedman, A. R. (2012). Extratropical cooling, interhemispheric thermal gradients, and tropical climate change. *Annual Review of Earth and Planetary Sciences*, *40*, 383–412.

Clarke, L., Edmonds, J., Jacoby, H., Pitcher, H., Reilly, J., & Richels, R. (2007). Scenarios of greenhouse gas emissions and atmospheric concentrations.

Fu, Y., Tai, A. P., & Liao, H. (2016). Impacts of historical climate and land cover changes on fine particulate matter (PM 2:5) air quality in East Asia between 1980 and 2010. *Atmospheric Chemistry & Physics*, *16*(16), 10,369–10,383.

Hansen, J., Lacis, A., Rind, D., Russell, G., Stone, P., Fung, I., et al. (1984). Climate sensitivity: Analysis of feedback mechanisms. In M. Ewing, J. E. Hansenand, & T. Takahashi (eds.), *Climate processes and climate sensitivity* (Vol. 5, pp. 130–163): AGU Geophysical Monograph.

Hoesly, R. M., Smith, S. J., Feng, L., Klimont, Z., Janssens-Maenhout, G., Pitkanen, T., et al. (2018). Historical (1750–2014) anthropogenic emissions of reactive gases and aerosols from the community emissions data system (CEDS). *Geoscientific Model Development*, *11*(1–41), 369–408.

Hu, N., & Liu, X. (2013). Modeling study of the effect of anthropogenic aerosols on late spring drought in South China. *Acta Meteorologica Sinica*, *27*(5), 701–715.

Huang, Y., Xia, Y., & Tan, X. (2017). On the pattern of $CO_2$ radiative forcing and poleward energy transport. *Journal of Geophysical Research: Atmospheres*, *122*, 10,578–10,593. https://doi.org/10.1002/2017JD027221

Hurrell, J. W., Hack, J. J., Shea, D., Caron, J. M., & Rosinski, J. (2008). A new sea surface temperature and sea ice boundary dataset for the community atmosphere model. *Journal of Climate*, *21*(19), 5145–5153.

Hwang, Y.-T., & Frierson, D. M. (2010). Increasing atmospheric poleward energy transport with global warming. *Geophysical Research Letters*, *37*, L24807. https://doi.org/10.1029/2010GL045440

Kloster, S., Dentener, F., Feichter, J., Raes, F., Lohmann, U., Roeckner, E., & Fischer-Bruns, I. (2010). A GCM study of future climate response to aerosol pollution reductions. *Climate Dynamics*, *34*(7-8), 1177–1194.

Lecœur, É., Seigneur, C., Pagé, C., & Terray, L. (2014). A statistical method to estimate PM2.5 concentrations from meteorology and its application to the effect of climate change. *Journal of Geophysical Research: Atmospheres*, *119*, 3537–3585. https://doi.org/10.1002/2013JD021172

Li, J. (2017). Comments on on the choice of average solar zenith angle. *Journal of the Atmospheric Sciences*, *74*(5), 1669–1676.

Li, J., Barker, H., Yang, P., & Yi, B. (2015). On the aerosol and cloud phase function expansion moments for radiative transfer simulations. *Journal of Geophysical Research: Atmospheres*, *120*, 12,128–12,142. https://doi.org/10.1002/2015JD023632

Li, J., Scinocca, J., Lazare, M., McFarlane, N., Von Salzen, K., & Solheim, L. (2006). Ocean surface albedo and its impact on radiation balance in climate models. *Journal of Climate*, *19*(24), 6314–6333.

Li, J., Wong, J., Dobbie, J., & Chylek, P (2001). Parameterization of the optical properties of sulfate aerosols. *Journal of the Atmospheric Sciences*, *58*(2), 193–209.

Ming, Y., & Ramaswamy, V. (2011). A model investigation of aerosol-induced changes in tropical circulation. *Journal of Climate*, *24*(19), 5125–5133.

Moss, R. H., Edmonds, J. A., Hibbard, K. A., Manning, M. R., Rose, S. K., Van Vuuren, D. P., et al. (2010). The next generation of scenarios for climate change research and assessment. *Nature*, *463*(7282), 747.
Myhre, G., Samset, B. H., Schulz, M., Balkanski, Y., Bauer, S., Berntsen, T. K., et al. (2013). Radiative forcing of the direct aerosol effect from Aerocom phase ii simulations. *Atmospheric Chemistry and Physics*, *13*(4), 1853–1877.
Räisänen, P., Barker, H. W., Khairoutdinov, M. F., Li, J., & Randall, D. A. (2004). Stochastic generation of subgrid-scale cloudy columns for large-scale models. *Quarterly Journal of the Royal Meteorological Society*, *130*(601), 2047–2067. A journal of the Atmospheric Sciences, applied meteorology and physical oceanography.
Riahi, K., Grübler, A., & Nakicenovic, N. (2007). Scenarios of long-term socio-economic and environmental development under climate stabilization. *Technological Forecasting and Social Change*, *74*(7), 887–935.
Rotstayn, L., Collier, M., Chrastansky, A., Jeffrey, S., & Luo, J.-J. (2013). Projected effects of declining aerosols in RCP4.5: Unmasking global warming?. *Atmospheric Chemistry and Physics*, *13*(21), 10,883–10,905.
Rotstayn, L. D., & Lohmann, U. (2002). Tropical rainfall trends and the indirect aerosol effect. *Journal of Climate*, *15*(15), 2103–2116.
Sand, M., Samset, B. H., Balkanski, Y., Bauer, S., Bellouin, N., Berntsen, T. K., et al. (2017). Aerosols at the poles: An Aerocom Phase II multi-model evaluation. *Atmospheric Chemistry and Physics*, *17*(19), 12,197–12,218.
Shindell, D. T., Lamarque, JF, Schulz, M., Flanner, M., Jiao, C., Chin, M., et al. (2013). Radiative forcing in the ACCMIP historical and future climate simulations. *Atmospheric Chemistry and Physics*, *13*(6), 2939–2974.
Smith, S. J., & Wigley, T. (2006). Multi-gas forcing stabilization with minicam. *The Energy Journal*, *27*, 373–391.
So, J., Yeh, S., Kim, M., & Park, R. (2014). Relationship of regional PM2.5 variations in East Asia and climate variability in the north pacific. In Agu fall meeting abstracts.
Srivastava, R., Ramachandran, S., Rajesh, T., & Kedia, S. (2011). Aerosol radiative forcing deduced from observations and models over an urban location and sensitivity to single scattering albedo. *Atmospheric Environment*, *45*(34), 6163–6171.
Van Vuuren, D. P., & Riahi, K. (2011). The relationship between short-term emissions and long-term concentration targets. *Climatic Change*, *104*(3-4), 793–801.
Wang, T., Li, S., Shen, Y., Deng, J., & Xie, M. (2010). Investigations on direct and indirect effect of nitrate on temperature and precipitation in China using a regional climate chemistry modeling system. *Journal of Geophysical Research*, *115*, D00K26. https://doi.org/10.1029/2009JD013264
Wang, Z., Lin, L., Yang, M., Xu, Y., & Li, J. (2017). Disentangling fast and slow responses of the East Asian summer monsoon to reflecting and absorbing aerosol forcings. *Atmospheric Chemistry and Physics*, *17*(18), 11075–11088.
Wang, Q., Wang, Z., & Zhang, H. (2017). Impact of anthropogenic aerosols from global, East Asian, and non-East Asian sources on East Asian summer monsoon system. *Atmospheric Research*, *183*, 224–236.
Wang, Z., Zhang, H., Jing, X., & Wei, X. (2013). Effect of non-spherical dust aerosol on its direct radiative forcing. *Atmospheric Research*, *120*, 112–126.
Wang, Z., Zhang, H., Li, J., Jing, X., & Lu, P. (2013). Radiative forcing and climate response due to the presence of black carbon in cloud droplets. *Journal of Geophysical Research: Atmospheres*, *118*, 3662–3675. https://doi.org/10.1002/jgrd.50312
Wang, Z., Zhang, H., & Lu, P. (2014). Improvement of cloud microphysics in the aerosol-climate model bcc_agcm2. 0.1 _cuace/aero, evaluation against observations, and updated aerosol indirect effect. *Journal of Geophysical Research: Atmospheres*, *119*, 8400–8417. https://doi.org/10.1002/2014JD021886
Williams, K., Jones, A., Roberts, D., Senior, C., & Woodage, M. (2001). The response of the climate system to the indirect effects of anthropogenic sulfate aerosol. *Climate Dynamics*, *17*(11), 845–856.
Wise, M., Calvin, K., Thomson, A., Clarke, L., Bond-Lamberty, B., Sands, R., et al. (2009). Implications of limiting $CO_2$ concentrations for land use and energy. *Science*, *324*(5931), 1183–1186.
Wu, T., Yu, R., & Zhang, F. (2008). A modified dynamic framework for the atmospheric spectral model and its application. *Journal of the Atmospheric Sciences*, *65*(7), 2235–2253.
Wu, T., Yu, R., Zhang, F., Wang, Z., Dong, M., Wang, L., et al. (2010). The Beijing climate center atmospheric general circulation model: description and its performance for the present-day climate. *Climate Dynamics*, *34*(1), 123.
Zhang, X. (2007). Aerosol over China and their climate effect. *Advances in Earth Science*, *22*(1), 12–16.
Zhang, H., Jing, X., & Li, J. (2014). Application and evaluation of a new radiation code under McICA scheme in bcc_agcm2. 0.1. *Geoscientific Model Development*, *7*(3), 737.
Zhang, H., Wang, Z., Wang, Z., Liu, Q., Gong, S., Zhang, X., et al. (2012). Simulation of direct radiative forcing of aerosols and their effects on East Asian climate using an interactive AGCM-aerosol coupled system. *Climate Dynamics*, *38*(7-8), 1675–1693.
Zhang, H., Zhao, S., Wang, Z., Zhang, X., & Song, L. (2016). The updated effective radiative forcing of major anthropogenic aerosols and their effects on global climate at present and in the future. *International Journal of Climatology*, *36*(12), 4029–4044.
Zhao, S., Zhang, H., Wang, Z., & Jing, X. (2017). Simulating the effects of anthropogenic aerosols on terrestrial aridity using an aerosol–climate coupled model. *Journal of Climate*, *30*(18), 7451–7463.
Zhou, C., Gong, S., Zhang, X., Liu, H., Xue, M., Cao, G., et al. (2012). Towards the improvements of simulating the chemical and optical properties of Chinese aerosols using an online coupled model—CUACE/Aero. *Tellus B: Chemical and Physical Meteorology*, *64*(1), 18965.
Zhou, C., Zhang, H., Zhao, S., & Li, J. (2017). Simulated effects of internal mixing of anthropogenic aerosols on the aerosol–radiation interaction and global temperature. *International Journal of Climatology*, *37*, 972–986.
Zhu, J., Penner, J. E., Lin, G., Zhou, C., Xu, L., & Zhuang, B. (2017). Mechanism of SOA formation determines magnitude of radiative effects. *Proceedings of the National Academy of Sciences*, *114*(48), 12685–12690.